Strain and charge carrier coupling in epitaxial graphene

Diedrich A. Schmidt, Taisuke Ohta, and Thomas E. Beechem

Phys. Rev. B **84**, 235422 — Published 5 December 2011

DOI: 10.1103/PhysRevB.84.235422

TITLE: Strain and charge carrier coupling in epitaxial graphene

Diedrich A. Schmidt[1,*], Taisuke Ohta[2,*], and Thomas E. Beechem[2]

[1] Department of Physical Chemistry II, Ruhr-University Bochum, Bochum, NRW 44780 Germany
[2] Sandia National Laboratories, Albuquerque, NM 87185 USA
CORRESPONDING AUTHORS: Diedrich.Schmidt@rub.de (DAS), tohta@sandia.gov (TO)

ABSTRACT:
We report a striking coupling between strain and carrier concentration variations at micro-meter scale in single layer graphene grown on silicon-carbide (SiC) (0001). The in-plane compressive strain (up to 0.4%) and carrier concentration are probed using Raman spectroscopy. We show that the large strain inhomogeneities in graphene initiate at the growth stage, and develop further by strain relaxation along the mismatched symmetry axes of the graphene and the underlying substrate. The strain relaxation is accompanied by a locally larger electron concentration, suggesting that charge transfer reduces the strain energy in the overall system. Our work establishes the strain and doping variations as coupled, intrinsic properties of epitaxial graphene growth on SiC(0001).

KEYWORDS: Epitaxial graphene, strain, Raman micro-spectroscopy, silicon carbide, low energy electron microscopy

PACS: 81.05.ue, 68.65.Pq, 68.60.Bs, 63.22.Rc

INTRODUCTION:
Graphene, a single layer of graphite, bears promise for a host of future electronics applications, owing to its excellent electronic,[1,2] thermal[3] and mechanical properties.[4] These properties, however, are exceptionally sensitive to external perturbations such as electric fields,[5] mechanical strain,[6-12] and charge transfer from surrounding molecules[13] and substrates.[1,2] Understanding the influence of mechanical strain, charge transfer, and particularly their interplay is important for epitaxial graphene on SiC, a materials combination envisioned for a diverse set of electronics applications.[14,15] Strain and electronic properties are coupled in materials,[16,17,18,19] thus modifying one will influence the other. For graphene and graphite, the interplay between strain and electronic properties has been discussed in terms of charge transfer and lattice constant variations. Examples include graphite intercalation compounds (GIC),[20] electron and hole puddles due to ripples,[21,22] and the predicted band gap opening in graphene.[11,12] Thus, exploiting the strain could lead to new possibilities of "strain engineering" in graphene.[23]

Despite its importance, our understanding of strain remains elusive for epitaxial graphene on SiC, especially what determines its magnitude, how it develops or relaxes, and how it influences the electronic properties. Raman spectroscopy is an ideal tool to address these issues as it is a direct probe

of phonon vibrations, and is sensitive to both the local stress and electronic properties. However, previous Raman studies of epitaxial graphene on SiC(0001) assumed that the phonon frequencies are modified only by strain.[24-28] Raman spectra in graphene are influenced to a minor extent by phonon softening, which depends on the carrier (or doping) concentration.[31-34] In addition, a broad range of compressive strain was reported for epitaxial graphene films,[25,26] which could result from the combination of the lattice mismatch[26] (~0.2% compressive [29]) and the difference of thermal expansion coefficients (TEC) between the graphene layer and SiC substrate (up to ~0.8% compressive [30]). The magnitude of strain is further obscured by subsequent reports suggesting that it could change during the different stages of graphene growth,[25,27] and vary locally depending on the underlying morphology of the SiC substrate.[24] Evidently, a proper evaluation of Raman spectra of epitaxial graphene has to take strain and carrier concentration into account.[35] As yet there is no comprehensive evaluation of Raman spectra considering both effects.

Here, using Raman spectroscopy, we study the local coupling between strain and carrier concentration within epitaxial monolayer (ML) graphene grown on 6H-SiC(0001). In addition to a large in-plane compressive strain (up to 0.4%) and its local variation at the micro-meter scale, we find a striking correlation between the strain and the carrier concentration; both of which depend on the growth mechanism of the graphene film. We offer phenomenological models to explain (1) why strain and doping couple in graphene based on the Fermi velocity change, and (2) how they depend on the growth-mechanism due to the underlying substrate topography. Our study sheds light on the development and relaxation of strain, as well as its correlation to local carrier concentration, which needs to be taken into account for electronics applications utilizing the graphene-SiC(0001) system.

EXPERIMENTAL DETAILS:

The graphene films (partial and full ML coverage) studied here were synthesized via argon (Ar)-assisted graphitization as described in Ref. 36. The samples were grown on n-type 6H-SiC(0001) (Si-face, ~0.1 Ω-cm, Cree, Inc.). Prior to graphene growth, the surface was hydrogen etched (45% H_2 – Ar mixture) at 1425 ˚C to remove any polishing damage. Graphene was grown in a high temperature furnace by first raising the temperature to 1200 ˚C in a 10% H_2 – Ar mixture, then to 1450-1600 ˚C in Ar at atmospheric pressure. The 1ML thickness of the graphene layer was confirmed using low-energy electron microscopy (LEEM) (Elmitec GmbH), supplementing the Raman spectroscopy.[37,38]

Confocal Raman microspectroscopy and AFM measurements were performed at the same sample location with a WITec Alpha300 RAS microscope. The Raman excitation wavelength of 532 nm, combined with a 100×/0.9 NA lens provided a diffraction-limited lateral resolution of ~360 nm. Raman spectra were corrected for a linear background before conducting spectral analysis. A *k*-means clustering algorithm was applied using commercially available software (WITec GmbH) and used an Euclidean distance metric to sort the spectral data into clusters, to minimize differences within a cluster, and maximize differences between clusters.[39-41] The averaged spectra from the *k*-means clusters were normalized to the TO(X) phonon in 6H-SiC(0001) at 768 cm^{-1} prior to peak fitting using Lorentzian line shapes for intensity, peak position, and full width half maximum (FWHM) characterization. All Raman

images have step sizes of 100 nm, with a scan size of 30 × 30 μm^2 (ML growth) or 12 × 12 μm^2 (sub-ML growth) and an integration time per pixel of 0.095 s (ML growth) and 0.212 s (sub-ML growth), with a spectral resolution of ~2.9 cm^{-1}. No laser damage was observed during the measurements.

RESULTS:

A. Inhomogeneous Raman spectra of epitaxial graphene

As-grown graphene films display substantial variation in their local Raman spectra, yet have a very homogeneous morphology. Figure 1(a) shows the flat and featureless AFM topography of a typical as-grown graphene film adjacent to two bunched steps in the middle of the images. Graphene exhibits three distinct Raman bands; the D- (~1350 cm^{-1}), G- (~1580 cm^{-1}), and 2D-bands (~2700 cm^{-1})[42,43] originate from defect-induced,[26] Γ-point,[44] and double-resonant[45] Raman scattering processes, respectively. The corresponding Raman intensity map of the G-band (integrated over 1580-1605 cm^{-1}) (Fig. 1(b)) and the false-color map after clustering analysis of Raman spectra (Fig. 1(c)) show substantial variation. The naming scheme of the clusters shown in Fig. 1(c) is based on the strain state of each region. Details of the assignments are described in the subsequent section, B. Quantifying the residual strain and carrier concentration. Briefly, RML stands for relaxed ML (cyan), PRML is partially relaxed ML (yellow), PSML is partially strained ML (blue), SML is strained ML graphene (green), and greater than 1ML coverage (red). The corresponding averaged spectrum from each cluster is shown in Fig. 1(e), together with the Raman spectra of bare SiC (black curve) for reference. The averaged spectra (Fig. 1(e)) highlight different Raman shifts for each 1ML graphene cluster.

We find that the local Raman shifts accompany the qualitative changes in AFM phase imaging. Figure 1(d) is a false-color overlay showing the direct correlation between the peak shift of the G-band (shown as a color contour) and the AFM phase map (shown in gray scale). For the G-band peak shift, blue denotes a shift to higher wavenumber, whereas yellow is unshifted from ω^0_G = 1582 cm^{-1}. AFM phase mapping clearly reveals additional features in the graphene films, which directly correlate with the Raman G-band shifts (Fig. 1(d)), and are not evident in the topography (Fig. 1(a)). This suggests that the observed variation of Raman spectra is correlated to the mechanical behavior of the graphene or the underlying SiC substrate. Concern of macroscopic ripples or delamination has been raised for graphene films on metal or SiC(000-1),[46,47] but they are not supported by the AFM topography of our 1ML graphene.

Analysis of the 2D-band FWHM in Fig. 1(e) allows us to determine graphene film thickness[42] and to exclude multilayer Raman spectra from further analysis. The narrow (FWHM = 37 cm^{-1}) and intense 2D peak of the SML spectra (Fig. 1(e), green curve), which is comparable to reported values for exfoliated graphene,[6,48] indicates ML film coverage; a broad and weaker 2D peak is observed for multilayer graphene near the step edges (Fig. 1(e), red curve). In addition, the ratio of the peak intensities, I_{2D}/I_G = ~0.4, from >1 ML coverage is lower than those of the ML coverage film, ~0.5 to ~0.6. The assignment of graphene thickness is consistent with our independent LEEM observations.[36,37,38]

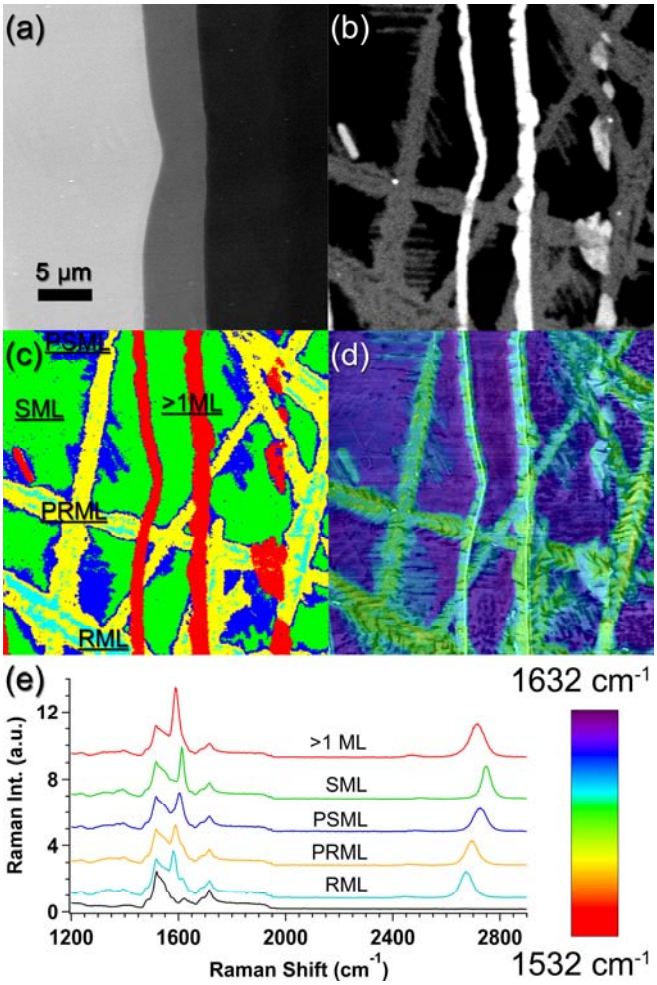

FIG. 1. Inhomogeneous Raman spectra in 1ML epitaxial graphene (color online). (a) AFM topography, (b) Raman G-band intensity map integrated over 1580-1605 cm^{-1}, (c) false-color Raman cluster map, (d) overlay of G-band peak position map (color scale below; blue: shift to higher wavenumber, yellow: unshifted with respect to ω^0_G = 1582 cm^{-1}) on AFM phase image shown in gray-scale, (e) average spectra from clusters in (c) with bare SiC (black) for reference; color coding same as in (c). Scan size is 30 × 30 μm^2. Labels in (c) and (e) correspond to each cluster categorized by its strain state. RML stands for relaxed ML (cyan); PRML, partially relaxed ML (yellow); PSML, partially strained ML (blue); SML, strained ML graphene (green); and greater than 1ML coverage (red). Note the lack of any significant defect-induced D-band for all clusters.

B. Quantifying the residual strain and carrier concentration

We interpret the shifts of the G- and 2D-band positions as resulting from both built-in compressive strain and charge transfer from the underlying substrate. The phonon frequencies in graphene can be shifted by strain[8-10] and carrier concentration,[32,49] with each effect separately determined using mechanically exfoliated graphene films and Raman spectroscopy. Assuming that the peak position shifts are a linear combination of the mechanical strain and carrier doping effects, we evaluated our spectra using the following relationship:

$$\omega_{G:2D} = \omega^0_{G:2D} + \Delta\omega^m_{G:2D} + \Delta\omega^e_{G:2D}$$

$\omega_{G:2D}$, $\omega^0_{G:2D}$, $\Delta\omega^m_{G:2D}$, and $\Delta\omega^e_{G:2D}$ are the measured Raman band frequency, unstrained and undoped Raman band frequency (ω^0_G = 1582 cm^{-1} and ω^0_{2D} = 2677 cm^{-1}),[43,48] and the changes in Raman band frequency due to mechanical strain (m) and carrier doping (e), respectively. G:2D stands for either G- or 2D-band.

We assume a biaxial strain state[50] neglecting the shear component (i.e. the shear deformation potential), and approximate the change in band frequency of the G- and 2D-bands as Mohiuddin *et al.*[8] by the following:

$$\Delta\omega^m_{G:2D} = -2\omega^0_{G:2D}\gamma_{G:2D}\varepsilon_{G:2D}$$

$\gamma_{G:2D}$ and $\varepsilon_{G:2D}$ are mode-dependent Grüneisen parameter and strain, respectively. The assumption of biaxial strain is supported because we do not detect any observable splitting of the G band, as would be expected for planar or uniaxial strain. We use the two-dimensional Grüneisen parameter γ_G = 2 for the G-band[51] and γ_{2D} = 2.8 for the 2D-band[8] to calculate the residual strain. In the following, we denote compressive strain as a negative value, and tensile as positive. Although there is discrepancy in the reported Grüneisen parameters, the values we use for γ_G and γ_{2D} are comparable to those recently reported from experiment[52] and first principles calculations[53]. We have verified that changes of 10% in the Grüneisen parameters (γ_G = 1.8 and γ_{2D} = 2.7 instead of γ_G = 2 and γ_{2D} = 2.8) only change the average charge carrier concentrations by about 0.15 × 10^{13} cm^{-2}, thus not affecting the overall discussions in the following.

The Raman shift by carrier doping is evaluated based on the empirical relationship of G- and 2D-band positions as a function of a carrier concentration reported by Das *et al.*[49] The overall carrier concentration of epitaxial graphene 1ML films on SiC(0001) prepared in a similar manner is reported to be ~1 × 10^{13} cm^{-2} (positive value is electron doping).[54] For the carrier concentration ranging between -0.6 × 10^{13} to 3 × 10^{13} cm^{-2}, the 2D-band frequency is almost invariant.[49] Because of the double resonant Raman scattering process for the 2D-band,[55] the difference in photon energy used for our and Das' experiments (532 nm vs. 514 nm) should red-shift our ω^0_{2D} (2D-band position without doping and strain) with respect to Das' by ~7.61 cm^{-1}. This leaves 2.01 cm^{-1} difference between our and Das' ω^0_{2D}, which is smaller than our spectrometer resolution. Note that ω^0_G = 1582 cm^{-1} for our measurement is also slightly different from what is reported in ref. 49. We therefore assume $\Delta\omega^e_{2D}$ = 2.01 cm^{-1} as a constant shift in our analysis. We verified that the change of ω^0_{2D} has only a minor effect (shifting ω^0_{2D} by 2 cm^{-1} results in a 6 x 10^{11} cm^{-2} change in carrier concentration) on the analysis described in the following.

The strain and carrier concentration display a striking correlation. Figs. 2 (a) and (c) show the calculated strain and carrier concentration maps determined from Raman spectra, respectively. Here regions of more than 1ML graphene are not shown (blacked out). We also find a very good correlation between Figs. 2(a) and (c) and the Raman cluster maps shown in Fig. 1 (c). Based on this correlation, we name

each cluster as follows. The cyan clusters in Fig. 1(c) indicate regions of relaxed ML (RML, cyan) graphene. Bounding the RML regions are areas of partially relaxed ML (PRML, yellow) that transition to partially strained ML (PSML, blue), followed by large areas of near-uniformly strained ML graphene (SML, green). The relative magnitude of the strain for each cluster is discussed in the following.

This correlation between the strain and carrier concentration maps is clearly seen in the corresponding histograms (Figs. 2(b) and (d)). The data points of each map are categorized by the clusters defined in Fig. 1 (c). The strain histogram (Fig. 2(b)) shows a perfect correlation to the cluster analysis (Fig. 1(c)), as expected. It is clear from Fig. 2(d) that the regions with more compressive strain (more blue in Fig. 2(a) or SML) correlate with regions of less electron concentration (more blue in Fig. 2(c)). The SML cluster (green bars in Fig. 2(d)) has an electron concentration roughly 1/3 less than the others.

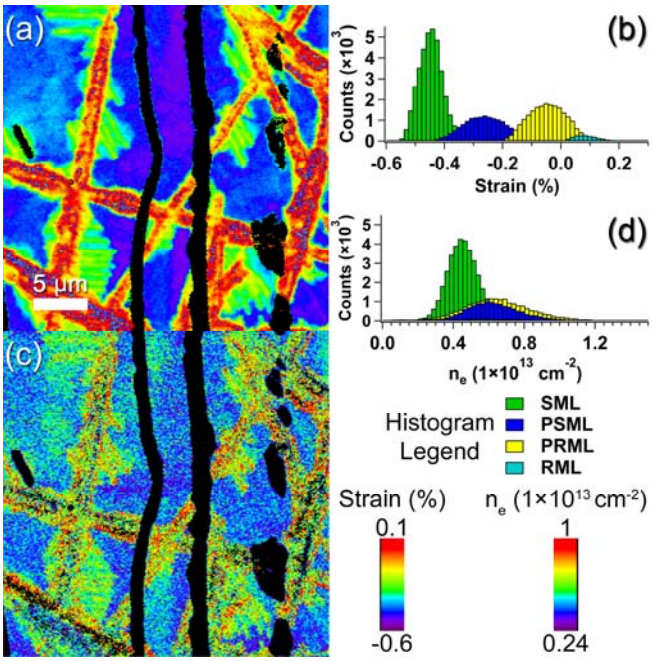

FIG. 2. Strain and carrier concentration mapping (color online). (a) Mechanical strain-field map, (b) histogram of strain values for (a) categorized by the clusters in Fig. 1(c), (c) electron concentration map, (d) histogram of electron concentrations for (c) categorized by the clusters in Fig. 1(c). Regions of more than 1ML graphene are not shown (blackened out in (a) and (c)). Scan size is 30 × 30 μm^2. Right bottom: legend for the histogram plots and color-bar scales for strain and carrier concentration.

C. Development and relaxation of the strain

To clarify the origins of the strain and carrier concentration inhomogeneities, we conducted Raman mapping of a partially graphitized sample (sub-ML coverage). The sample includes two major growth features: step-flow growth initiated at a macroscopic step, which converts three Si-C bilayers of SiC to a single sheet of graphene, and irregular growth, which decorates a single Si-C bilayer step with narrow domains of 1ML graphene.[36,56,57] They are conspicuous in the AFM phase map (Fig. 3(a)) and Raman cluster map (Fig. 3(b)), and are schematically illustrated in Figs. 3(e) & (f).

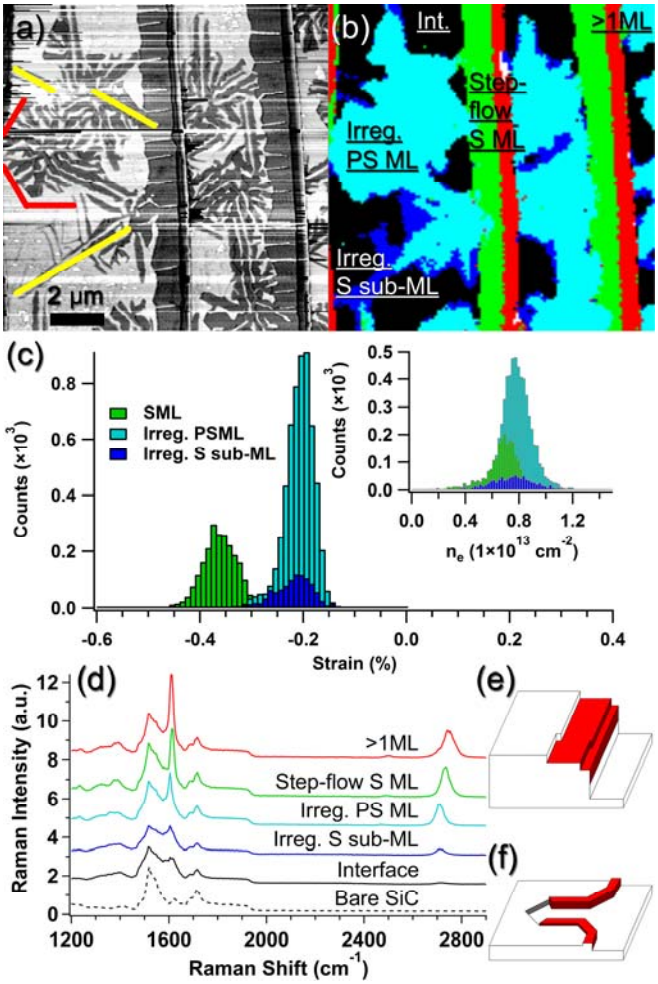

FIG. 3. The surface of partially graphitized SiC (color online). (a) AFM phase map, (b) false-color Raman cluster map, (c) strain and carrier concentration (inset) histograms of the clusters shown in (b), (d) average spectra from strain clusters in (b) with bare SiC (dashed curve) for reference; color coding same as (b), (e-f) schematic of the step-flow and irregular growth mode fronts, respectively. Scan size in (a) and (b) is 12 × 12 μm^2. Labels of clusters in (b) correspond to the spectra shown in (d).

The false-color Raman cluster map (Fig. 3(b)) and corresponding spectra (Fig. 3(d)) clearly distinguish between the interface buffer layer (black),[36] the irregular growth fronts (blue and cyan), and the step-flow growth (green), as well as areas of more than 1 ML (red). The black regions in Fig. 3(b) are assigned to the interface layer because of the partially developed G-band compared to the bare SiC spectra (black dotted line in Fig. 3(d)), as well as the lack of a 2D-band. The absence of the 2D-band is likely due to the strong covalent bonds grafting the interface layer to the substrate,[58] which destroys the π-π interactions required to satisfy the double-resonant Raman scattering conditions for the 2D-band.[45] Conversely, the irregular growth and the step-flow growth regions have much stronger 2D-bands indicating in-plane π-π interactions as the graphene ML is established above the interface layer.

Histograms of the strain and carrier concentration for each cluster are shown in Fig. 3(c) and its inset, respectively. The two growth fronts result in very different strain states: step-flow growth makes larger compressive strain than irregular growth in graphene. This result suggests that the magnitude of strain is established during the growth, and strongly depends on the growth mechanism. Comparing the strain and carrier concentration histograms of Fig. 3(c), it is clear the strain-carrier correlation for sub-ML graphene follows the same behavior as for full ML graphene shown in Fig. 2(d). The cluster with larger strain (SML) results in lower carrier concentration. We also find that during the early stages of growth, graphene is slightly more doped while having less strain variation than the full coverage sample.

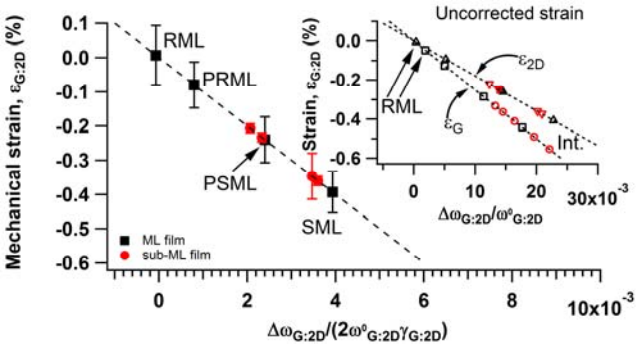

FIG. 4. Residual mechanical strain *vs*. normalized relative peak shift as determined from the G- and 2D-band peak shifts for sub-ML (red) and ML coverage (black) (color online). Inset: uncorrected strain *vs*. relative peak shift not considering carrier concentration dependence of the Raman peak shift. Circles and squares correspond to G-band positions, and up- down-triangles to 2D-band positions. The interface (Int.) and relaxed monolayer (RML) data points are noted for reference. The dashed lines are linear fits to the data points, with their slopes proportional to the Grüneisen parameters for the G- and 2D-bands.

A direct comparison of the strain between sub-ML and ML coverage sheds light on the strain development during graphene growth. The mechanical strains for each cluster from sub-ML (red markers) and ML coverage samples (black markers) are summarized in Fig. 4 (see Fig. S2 for the Raman peak positions of each cluster), where we have taken the effects of the carrier concentration on the shifts of the G- and 2D-bands into consideration. We find that the total mechanical strain varies from 0% to ~0.4% compressive. Note that the lattice[26] and thermal expansion coefficient (TEC) mismatches between the graphene layer and SiC substrate could result in up to ~0.2% compressive[29] and ~0.8% compressive strain[30], respectively. The RML (full ML coverage) has peak positions that compare favorably to that of exfoliated graphene, indicating full strain relaxation. The PSML regions (irregular growth for sub-ML coverage) can be primarily attributed to the lattice mismatch, with a maximum of ~0.2% compressive strain. On the other hand, SML regions (step-flow growth in sub-ML coverage) are influenced by both the lattice constant and TEC mismatches. Yet, the ~0.4% total compressive strain of the SML regions is considerably smaller than the ~0.8% compressive strain that could result from the difference in TEC alone, suggesting that some level of strain relaxation occurs in all clusters.

It was previously shown that step-flow growth takes place at step bunches of the SiC substrate (shown schematically in Fig. 2(f)).[36] The resulting graphene layer is therefore geometrically pinned by the growth fronts and the bunched steps of the SiC. In contrast, irregular growth fronts (illustrated in Fig. 2(g)) are formed along single SiC bilayer height steps, and involve diffusion of carbon atoms on the interface layer surface. As a result, graphene layers formed via irregular growth is therefore less likely to be chemically bound or pinned at the growth front. We postulate that the larger compressive strain at the step-flow growth fronts is associated with this geometrical constraint. This idea is further examined in the discussion that follows.

Also shown in the inset of Fig. 4 is the strain *vs*. relative peak shift not considering the carrier concentration dependence of the Raman peak positions. In other words, the strains are calculated using the measured G- and 2D-band positions, the reference G- and 2D-band positions (ω^0_G and ω^0_{2D}), and their Grüneisen parameters $\gamma_G = 2$ and $\gamma_{2D} = 2.8$. This leads to different values of the strain, ε_G and ε_{2D}. For example, the RML data points for the G- and 2D-bands have different strain values (see inset, Fig. 4). Our analysis accounts for this discrepancy by using the carrier concentration dependent shifts in addition to the shift due to mechanical strain to describe the entire Raman spectra.

Close examination of the irregular growth fronts (Fig. 3(a)) and the motif of the strain relaxed regions (RML, Fig. 1(c)) yield further insight into the mechanism of strain relaxation. In Fig. 3(a), the irregular growth fronts are aligned ±30° relative to horizontal (yellow lines drawn along [1-100] directions of the SiC substrate[36]), whereas the PSML clusters (cyan) are bounded by multiples of 60° (red lines drawn along [11-20] directions). The strain-relief lines (yellow and cyan) in Fig. 1(c) are oriented at multiples near 30° relative to each other. Given the 30° rotated symmetry of the interface and ML films relative to the substrate,[58,59] we presume that the symmetry of the irregular growth fronts in the sub-ML coverage (Fig. 3) and strain-relaxed lines in the ML coverage films (Fig. 1) play a role in how graphene films relax their strain.

DISCUSSION:

The striking correlation between the strain and carrier concentration variations found in epitaxial 1ML graphene on SiC(0001) leads to fundamental questions: (1) *why are strain and doping coupled*, (2) *how can a continuous film have regions of varying strain and carrier concentration*, and (3) *why do the strain state and carrier concentration depend on the growth-mode*? Owing to the combination of mismatched lattice constants[26] (~0.2%) and TECs[30] (up to ~0.8%) between graphene and the underlying substrate, the system should exhibit an overall compressive strain. Nonetheless, the measured carrier concentration variations (4 - 6 x 10^{12} cm^{-2} and 6 - 8 x 10^{12} cm^{-2} for ML and sub-ML coverage samples) correspond to ~50 meV variation of the Fermi-energy (the energy separation between the Fermi-level and charge neutrality point), which directly translates to a surface potential variation.[60] Ordinarily, a continuous and conductive film[61] would not sustain such a large potential variation across the surface.

In the following, we propose phenomenological models to explain (1) the observed *strain-doping relation*, which is based on changes in the Fermi velocity and size of the Brillouin zone (BZ) due to strain, and (2) the *growth-mode dependent strain and doping variations*, which are due to the pinning of the domain boundary and atomic-scale corrugation resulting from the underlying substrate topography.

Strain-doping correlation

It has long been known that the in-plane carbon bond length varies as a function of the carrier concentration in graphite intercalation compounds (GICs).[20,62,63] In GICs, electrons (or holes) are transferred from dopants to the antibonding π* state (the bonding π state) of a graphite host, leading to an increase (decrease) in the carbon bond length. The increase in the carbon bond length for an electron concentration of 1 x 10^{13} cm^{-2} in GICs is only ~0.02%,[31] which is one order of magnitude smaller than our measured strain. For epitaxial graphene on SiC, the situation is complicated since the edges of a graphene domain are expected to be pinned to the underlying substrate, which is different from the simple doping of exfoliated graphene or GICs with mechanically free boundaries.

One way of explaining the observed strain-doping relation is to assume that the Fermi velocity (v_F) varies with the carbon bond length. Fig. 5 (a) illustrates the proposed model. The inner cones (blue) represent the π and π* states (Dirac cone) of unstrained, doped 1ML graphene (i.e. relaxed monolayer, or RML). Applying compressive stress reduces the carbon bond length, resulting in both a larger BZ and overlap integral, thus increasing v_F. Even if the Fermi-energy is unchanged, the larger v_F effectively reduces the carrier concentration because the opening of the cone becomes smaller for doped graphene. In Fig. 5(a), this is depicted as the outer cones (green) representing compressively strained and doped 1ML graphene (i.e. SML). The green cone has a smaller opening than the blue one, illustrating the smaller electron concentration for a compressed state. This model satisfies the system's driving force to make the surface potential, i.e. Fermi-energy, uniform while allowing the carrier concentration to fluctuate across the surface. Note that this v_F renormalization does not have much of an effect on undoped graphene as the Fermi level resides close to the charge neutrality point. This simple geometrical model is based on how v_F, Fermi energy, and the size of the BZ depend on the in-plane lattice constant.

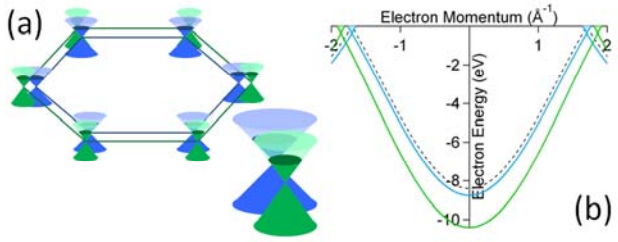

FIG. 5. A model accounting for the strain-doping correlation based on v_F renormalization. (a) Schematic illustration of the π and π* states (Dirac cone) for 1ML graphene with and without compressive strain. Inner cones (blue) show unstrained, doped 1ML, and outer cones (green) compressively strained, doped 1ML (corresponding to the cases of, for example, RML and SML, respectively). Varying the v_F changes the opening of the cones, thus modifying the carrier concentration for the doped graphene. (b) Tight binding (TB) band structure for unstrained (inner band, blue) and compressively strained (outer band,

green) 1ML for the parameters described in the text. The dash line is the unstrained, undoped case. The electron energy is plotted with respect to the Fermi level.

To verify this simple model, we calculate the in-plane lattice constant change for two carrier concentrations using a one-orbital tight binding (TB) model adopted from ref. 64. To connect the overlap integral and the carbon bond length, we assumed that the overlap integral changes by the inverse square of the lattice constant.[65,66] The correlation between the carrier concentration and the lattice constant can be seen in the following example. With a lattice constant of 2.46 Å, a Fermi-energy of 0.36 eV, and an orbital overlap of -2.8 eV, the calculated electron concentration is 5.8 x 10^{12} cm^{-2}. Reducing the lattice constant to 2.25 Å (with an unchanged Fermi-energy of 0.36 eV) yields an orbital overlap of -3.35 eV, and an electron concentration of 4.9 x 10^{12} cm^{-2}. This corresponds to a reduction of the lattice constant by 8.5%. The measured compressive strain of ~0.4% falls in between the *ab-initio* calculation (~0.02% increase of the carbon bond length)[31] and the simple TB model.

This simplified TB model qualitatively accounts for the measured strain-doping correlation. In reality, the assumption of a uniform surface potential (or Fermi-energy) for all the clusters would not strictly hold. It was recently reported that the surface potential of epitaxial 1ML graphene can vary locally by at least 12 meV.[67] Thus, this simple TB model would suggest the upper bound of the strain.

Growth-mode dependent strain and doping variations

Our analysis of the Raman spectroscopy measurements reveals growth-mode dependent strain and doping variations. In the previous section, we postulated that this strain variation is associated with the geometrical constraint resulting from the pinning of the graphene domain boundaries. In this section, we explore the atomic–scale origins behind why the strain state and the carrier concentration depend on the growth mechanism. We consider the atomic-scale topographic corrugation (or rippling) of graphene that could result from the underlying substrate morphology. This conjecture provides a qualitative description of how the strain state and carrier concentration are linked to a particular growth-mode.

It is predicted that the lattice deformation by rippling in graphene could give rise to localized electron or hole doped regions (electron and hole puddles).[21,22] Kim and Castro Neto have shown that due to the orbital rehybridization, a curved geometry promotes doping of graphene with electrons in a bumpier region and holes in a flatter region.[22] Epitaxial graphene on SiC(0001) indeed exhibits corrugated geometry at the atomic-scale because of the underlying interface buffer layer topography.[68] However, such corrugation was not considered in previous studies of strain in this system.

We begin the discussion with our experimental result that step-flow growth fronts develop larger compressive strain in graphene, while irregular ones result in smaller strains. In our previous work,[36] we have shown that irregular growth fronts occurs in the carbon diffusion-limited regime on the interface layer surface, which has large atomic-scale corrugations.[68] As discussed earlier, it is reasonable to assume that epitaxial graphene produced via irregular growth has large corrugations following the rough

topography of the underlying substrate.[68] On the other hand, step-flow growth converts three Si-C bilayers of SiC to 1ML of graphene, and simultaneously produces the interface layer. Step-flow growth is therefore less likely to be influenced by the underlying interface layer topography. Consequently, graphene made via irregular growth should have a bumpier morphology, and thus more electron doping, according to ref. 22. Conversely, flatter graphene films grown by step flow would result in less electron doping. This scenario is supported by our result shown in Figs. 3 (b) and (c), where irregular growth regions (PSML) display higher electron concentration than regions of step-flow growth (SML).

Corrugations make the actual length of a film larger than the projected surface length, and could thereby contribute to strain relaxation. We calculated the expected difference in the length of a graphene sheet based on the reported surface roughness of 1ML graphene on SiC(0001) (RMS roughness of ~0.01 nm)[68] compared to the flat surface. This amounts to only ~0.04%, which means that the atomic-scale rippling cannot fully account for the ~0.15% difference of strains between PSML and SML that we observed in the Raman measurement shown in Fig. 3(c).

Based on this model, we speculate that the difference in the strains for two different growth modes originates from the combination of the pinning of graphene domain boundaries and the atomic-scale corrugations of the graphene films, both of which are a consequence of the underlying substrate morphology. This conjecture also suggests that irregular growth regions could be more corrugated than step-flow growth regions, thus providing another consequence of the coupled strain, carrier concentration, and growth-modes, which could be verified using other characterization tools.

Finally, we comment on the limitations of our Raman analysis and our postulated models. So far, we have considered only a linear combination of the strain and carrier concentration in both our analysis of the Raman spectra and our models. In reality however, there must be a cross correlation term that influences the strain and doping simultaneously. Another limitation of our Raman analysis stems from the accuracy of the Grüneisen parameters, γ_G and γ_{2D}, as we discussed in the Result section. A more accurate determination of the local carrier concentration, as well as the strain, will rely on more precise measurements of the reported Grüneisen parameters. We also recognize that the two models presented in this section, based on the Fermi velocity renormalization and atomic-scale rippling, would be intertwined, and need further studies. Another issue that is not discussed in this paper includes the absence of macroscopic rippling or delamination of 1ML graphene on SiC(0001), which is observed for graphene growth on metals.[46]

Overall, a comprehensive understanding of this system would require more sophisticated analyses, for example *ab-initio* calculations. Yet theoretical studies of the graphene/SiC(0001) system remain difficult because of the large superstructures and continued debate over the interface structure.[69] The models presented here provide qualitative pictures for all our experimental results, and account for the previously reported strain evolution during graphene growth,[25,27] as well as the morphology dependent strain variations.[24] Our work highlights the importance of understanding the strain state, its

dependence on the growth mechanism, and the resulting complications that affect charge transfer, and hence the electronic properties of epitaxial graphene on SiC(0001).

CONCLUSION:

We have studied the strain and carrier concentration variations in single layer graphene on SiC(0001) using Raman spectroscopy. The strain and the carrier concentration display striking correlation, suggesting that the interrelated strain and doping variations are inherent to this system. The strain originates from the combination of lattice mismatch and the difference in thermal expansion coefficients between the graphene overlayer and SiC substrate, while the exact amount of strain depends on the growth mechanisms and strain relaxation. The specific growth mechanism thus ultimately influences both how strain develops and how charges transfer. Our work sheds light on the wide variations of the reported strain and electronic properties of epitaxial graphene on SiC(0001), and underscores the need for a comprehensive understanding of the strain-doping relationship.

ACKNOWLEDGMENT:

DAS thanks M. Havenith for use of experimental equipment. The Raman microscope was supported by BMBF grant 05KS7PC2. DAS acknowledges support within the BMBF funded project. This work was partly supported by the LDRD program at SNL, and the US DOE Office of Basic Energy Sciences, Division of Materials Science and Engineering (DE-AC04-94AL85000). A portion of this work was performed at CINT (Contract No. DE-AC04-94AL85000). We are grateful to E. Bründermann, N. Bartelt, P. Feibelman, L. Biedermann, S. Howell, G. Kellogg, T. Friedmann, and B. Swartzentruber for stimulating discussions; G. Copeland for sample preparation and characterization; and F. Ballout for assistance in image processing. SNL is a multi-program laboratory managed and operated by Sandia Corporation, a wholly owned subsidiary of Lockheed Martin Corporation, for the U.S. DOE National Nuclear Security Administration under contract DE-AC04-94AL85000.

REFERENCES:

1. X. Du, I. Skachko, F. Duerr, A. Luican, and E. Y. Andrei, Nature **462**, 192 (2009).
2. K. I. Bolotin, F. Ghahari, M. D. Shulman, H. L. Stormer, and P. Kim, Nature **462**, 196 (2009).
3. A. A. Balandin, S. Ghosh, W. Bao, I. Calizo, D. Teweldebrhan, F. Miao, and C. N. Lau, Nano Letters **8**, 902 (2008).
4. C. Lee, X. Wei, J. W. Kysar, and J. Hone, Science **321**, 385 (2008).
5. K. S. Novoselov, A. K. Geim, S. V. Morozov, D. Jiang, Y. Zhang, S. V. Dubonos, I. V. Grigorieva, and A. A. Firsov, Science **306**, 666 (2004).
6. Z. H. Ni, T. Yu, Y. H. Lu, Y. Y. Wang, Y. P. Feng, and Z. X. Shen, ACS Nano **2**, 2301 (2008).
7. W. Bao, F. Miao, Z. Chen, H. Zhang, W. Jang, C. Dames, C. N. Lau, Nature Nanotechnology **4**, 562 (2009).

8. T. M. G. Mohiuddin, A. Lombardo, R. R. Nair, A. Bonetti, R. Savini, R. Jalil, N. Bonini, D. M. Basko, C. Galiotis, N. Marzari, K. S. Novoselov, and A. K. Geim, Phys. Rev. B **79**, 205433 (2009).
9. M. Huang, H. Yan, C. Chen, D. Song, T. F. Heinz, and J. Hone, Proc. Natl. Acad. Sci. USA **106**, 7304 (2009).
10. M. Huang, H. Yan, T. F. Heinz, and J. Hone, Nano Letters DOI: 10.1021/nl102123c (2010).
11. G. Cocco, E. Cadelano, and L. Colombo, Phys. Rev. B **81**, 241412 (2010).
12. F. Guinea, M. I. Katsnelson, and A. K. Geim, Nature Physics 6, 30 (2010).
13. F. Schedin, A. K. Geim, S. V. Morozov, E. W. Hill, P. Blake, M. I. Katsnelson, K. S. Novoselov, Nature Materials 6, 652 (2007).
14. A. K. Geim, Science **324**, 1530 (2009), and Y. Lin, A. Valdes-Garcia, S. Han, D. B. Farmer, I. Meric, Y. Sun, Y. Wu, C. Dimitrakopoulos, A. Grill, Ph. Avouris, K. A. Jenkins, Science **332**, 1294 (2011).
15. Y.-M. Lin, C. Dimitrakopoulos, K. A. Jenkins, D. B. Farmer, H.-Y. Chiu, A. Grill, and Ph. Avouris, Science **327**, 662 (2010).
16. J. C. Bean, Science **230**, 127 (1985).
17. G. C. J. Osbourn, Appl. Phys. **53**, 1586 (1982).
18. S. Nakamura, Science **281**, 956 (1998).
19. P. Waltereit, O. Brandt, A. Trampert, H. T. Grahn, J. Menniger, M. Ramsteiner, M. Reiche, and K. H. Ploog, Nature **406**, 865 (2000).
20. D. E. Nixon, G. S. Parry, J. Physics C: Solid State Physics, **2**, 1732 (1969).
21. L. Brey and J. J. Palacios, Phys. Rev. B **77**, 041403(R) (2008).
22. Eun-Ah Kim and A. H. Castro Neto, Europhysics Letters **84**, 57007 (2008).
23. V. M. Pereira and A. H. Castro Neto, Phys. Rev. Lett. **103**, 046801 (2009).
24. J. A. Robinson, C. P. Puls, N. E. Staley, J. P. Stitt, M. A. Fanton, K. V. Emtsev, T. Seyller, and Y. Liu, Nano Letters **9**, 964 (2009).
25. N. Ferralis, R. Maboudian, and C. Carraro, Phys. Rev. Lett. **101**, 156801 (2008).
26. Z. H. Ni, W. Chen, X. F. Fan, J. L. Kuo, T. Yu, A. T. S. Wee, and Z. X. Shen, Phys. Rev. B **77**, 115416 (2008).
27. N. Ferralis, J. Kawasaki, R. Maboudian, and C. Carraro, Appl. Phys. Lett. **93**, 191916 (2008).
28. N. Ferralis, Journal of Materials Science **45**, 5135 (2010).
29. The lattice constants of graphene and SiC are aG = 2.461 Å and aSiC = 3.073 Å, respectively. Assuming a commensurate supercell with size of aG×13 (31.993 Å) or aSiC×(√3×6) (31.936 Å), the lattice mismatch results in approximately 0.2% compressive strain for the graphene layer.
30. The linear thermal expansion coefficients α of graphene and SiC are ~-0.98x10^{-6}/°C and ~4.9x10^{-6}/°C, respectively. By cooling down from the growth temperature (~1400 °C) to room temperature, the substrate should contract by (αSiC-αG) × 1400 °C ~ 0.8% with respect to graphene. References: N. Mounet, and N. Marzari, Phys. Rev. B **71**, 205214 (2005). Z. Li, R. C. Bradt, J. American Ceramic Soc. **69**, 863 (1986).
31. M. Lazzeri and F. Mauri, Phys. Rev. Lett. **97**, 266407 (2006).
32. S. Pisana, M. Lazzeri, C. Cashiraghi, K. S. Novoselov, A. K. Geim, A. C. Ferrari, and F. Mauri, Nature Materials **6**, 198 (2007).
33. J. Yan, Y. Zhang, P. Kim, and A. Pinczuk, Phys. Rev. Lett. **98**, 166802 (2007).

34. R. Yang, Q. S. Huang, X. L. Chen, G. Y. Zhang, and H.-J. Gao, J. Appl. Phys. **107**, 034305 (2010).
35. J. Röhrl, M. Hundhausen, F. Speck, Th. Seyller, Materials Science Forum **645-648**, 603 (2010).
36. T. Ohta, N. C. Bartelt, S. Nie, K. Thürmer, and G. L. Kellogg, Phys. Rev. B **81**, 121411(R) (2010).
37. H. Hibino, H. Kageshima, F. Maeda, M. Nagase, Y. Kobayashi, and H. Yamaguchi, Phys. Rev. B **77**, 075413 (2008).
38. T. Ohta, F. El Gabaly, A. Bostwick, J. L. McChesney, K. V. Emtsev, A. Schmid, T. Seyller, K. Horn, and E. Rotenberg, New J. Physics **10**, 023034 (2008).
39. J. B. McQueen, Proceedings of the Fifth Berkeley Symposium on Mathematical Statistics **1**, 281 (1967).
40. T. Kanungo, D. M. Mount, N. S. Netanyahu, C. D. Piatko, R. Silverman, and A. Y. Wu, IEEE Trans. Pattern. Anal. Mach. Intell. **24**, 881 (2002).
41. C. M. Bishop, *Pattern Recognition and Machine Learning* (Springer, New York, 2006) pp. 424-430.
42. A. C. Ferrari, J. C. Meyer, V. Scardaci, C. Casiraghi, M. Lazzeri, F. Mauri, S. Piscanec, D. Jiang, K. S. Novoselov, S. Roth, and A. K. Geim, Phys. Rev. Lett. **97**, 187401 (2006).
43. L. M. Malard, M. A. Pimenta, G. Dresselhaus, and M. S. Dresselhaus, Physics Reports **473**, 51 (2009).
44. F. Tuinstra and J. Koenig, J. Chem. Phys. **53**, 1126 (1970).
45. C. Thomsen and S. Reich, Phys. Rev. Lett. **85**, 5214 (2000).
46. A. T. N'Diaye, R. van Gastel, A. J. Martínez-Galera, J. Coraux, H. Hattab, D. Wall, F.-J. zu Meyer zu Heringdorf, M. Horn-von Hoegen, J. M. Gómez-Rodríguez, B. Poelsema, C. Busse, and T. Michely, New Journal of Physics **11**, 113056 (2009).
47. L. B. Biedermann, M. L. Bolen, M. A. Capano, D. Zemlyanov, and R. G. Reifenberger, Phys. Rev. B **79**, 125411 (2009).
48. D. Graf, F. Molitor, K. Ensslin, C. Stampfer, A. Jungen, C. Hierold, and L. Wirtz, Nano Letters **7**, 238 (2007).
49. A. Das, S. Pisana, B. Chakraborty, S. Piscanec, S. K. Saha, U. V. Waghmare, K. S. Novoselov, H. R. Krishnamurthy, A. K. Geim, A. C. Ferrari, and A. K. Sood, Nature Nanotechnology **3**, 210 (2008).
50. The assumption of biaxial strain is based on the fact that the Raman spectra vary at the length scale of μm (shown in Figs. 1 and 2), much larger than the spot size of the laser in our confocal Raman microscope.
51. C. Thomsen, S. Reich, and P. Ordejón, Phys. Rev. B **65**, 073403 (2002).
52. F. Ding, H. Ji, Y. Chen, A. Herklotz, K. Dörr, Y. Mei, A. Rastelli, and O. G. Schmidt, Nano Letters **10**, 3453 (2010).
53. Y. C. Cheng, Z. Y. Zhu, G. S. Huang, and U. Schwingenschlögl, Phys. Rev. B. **83**, 115449 (2011).
52. K. V. Emtsev, A. Bostwock, K. Horn, J. Jobst, G. L. Kellogg, L. Ley, J. L. McChesney, T. Ohta, S. A. Reshanov, J. Röhrl, E. Rotenberg, A. K. Schmid, D. Waldmann, H. Weber, and T. Seyller, Nature Materials **8**, 203 (2009).
53. L. M. Malard, J. Nilsson, D. C. Elias, J. C. Brant, F. Plentz, A. S. Alves, A. H. Castro Neto, and M. A. Pimenta, Phys. Rev. B **76**, 201401 (2007).
54. V. Borovikov, and A. Zangwill, Phys. Rev. B **80**, 121406(R) (2009).
55. M. L. Bolen, S. E. Harrison, L. B. Biedermann, and M. A. Capano, Phys. Rev. B **80**, 115433 (2009).
56. K. V. Emtsev, F. Speck, T. Seyller, L. Ley, and J. D. Riley, Phys. Rev. B **77**, 155303 (2008).

57. Th. Seyller, A. Bostowick, K. V. Emtsev, K. Horn, L. Ley, J. L. McChesney, T. Ohta, J. D. Riley, E. Rotenberg, and F. Speck, Phys. Stat. Sol. (b) **245**, 1436 (2008).
58. Y-J. Yu, Y. Zhao, S. Ryu, L. E. Brus, K. S. Kim, P. Kim, Nano Lett., **9**, 3430 (2009).
59. W. Pan, S. W. Howell, A. J. Ross III, T. Ohta, and T. A. Friedmann Appl. Phys. Lett., **97**, 252101 (2010).
60. R. J. Nemanich, S. A. Solin, D. Gúerard, Phys. Rev. B **16**, 2965–2972 (1977)
61. L. Pietronero and S. Strässler, Phys. Rev. Lett. **47**, 593–596 (1981).
62. A. Bostwick, T. Ohta, T. Seyller, K. Horn, and E. Rotenberg, Nature Physics **3**, 36 (2007).
63. W. A. Harrison, Electronic Structure and the Properties of Solids: The Physics of the Chemical Bond, Dover Publications, Inc. (1980).
64. W. A. Harrison, Phys. Rev. B **27**, 3592–3604 (1983).
65. A. E. Curtin, M. S. Fuhrer, J. L. Tedesco, R. L. Myers-Ward, C. R. Eddy, Jr., and D. K. Gaskill, Appl. Phys. Lett. **98**, 243111 (2011).
66. P. Lauffer, K. V. Emtsev, R. Graupner, Th. Seyller, L. Ley, S. A. Reshanov, H. B. Weber, Phys. Rev. B **77**, 155426 (2008).
67. Y. Qi, S. H. Rhim, G. F. Sun, M. Weinert, L. Li, Phys. Rev. Lett. **105**, 085502 (2010).
68. See EPAPS Document No. [number to be inserted by publisher] for supplemental material.